Mesoscale observations of Joule heating near an auroral arc and ion-neutral collision frequency in the polar cap *E* region

M. J. Kosch,[1,2] I. Yiu,[3] C. Anderson,[4] T. Tsuda,[1] Y. Ogawa,[5] S. Nozawa,[1] A. Aruliah,[3] V. Howells,[6] L. J. Baddeley,[7] I. W. McCrea,[6] and J. A. Wild[2]

Received 17 August 2010; revised 25 February 2011; accepted 7 March 2011; published 21 May 2011.

[1] We report on the first mesoscale combined ionospheric and thermospheric observations, partly in the vicinity of an auroral arc, from Svalbard in the polar cap on 2 February 2010. The EISCAT Svalbard radar employed a novel scanning mode in order to obtain *F* and *E* region ion flows over an annular region centered on the radar. Simultaneously, a colocated Scanning Doppler Imager observed the *E* region neutral winds and temperatures around 110 km altitude using the 557.7 nm auroral optical emission. Combining the ion and neutral data permits the *E* region Joule heating to be estimated with an azimuthal spatial resolution of ~64 km at a radius of ~163 km from the radar. The spatial distribution of Joule heating shows significant mesoscale variation. The ion-neutral collision frequency is measured in the *E* region by combining all the data over the entire field of view with only weak aurora present. The estimated ion-neutral collision frequency at ~113 km altitude is in good agreement with the MSIS atmospheric model.

Citation: Kosch, M. J., et al. (2011), Mesoscale observations of Joule heating near an auroral arc and ion-neutral collision frequency in the polar cap *E* region, *J. Geophys. Res.*, *116*, A05321, doi:10.1029/2010JA016015.

1. Introduction

[2] At high latitudes, magnetosphere-ionosphere coupling is achieved through large-scale field-aligned current (FAC) systems [e.g., *Iijima and Potemra*, 1976; *Kosch and Nielsen*, 2001; *Zmuda and Armstrong*, 1974]. In the premagnetic midnight dusk sector, downward FACs flow equatorward of the upward return currents and vice versa in the postmagnetic midnight dawn sector. The large-scale morphology of the FACs is controlled by the interplanetary magnetic field (IMF) B_z and B_y components [*Weimer*, 2001]. For B_z negative the statistical strength of the FAC is controlled by the amplitude of B_z [*Kosch and Nielsen*, 2001]. For B_z positive, the FAC strength weakens and breaks up into multiple zones [*Friis-Christensen et al.*, 1985; *Iijima and Shibaji*, 1987]. These currents close via poleward (equatorward) ionospheric Pedersen currents in the dusk (dawn) sector and dissipate energy via Joule heating, which is largely an *E* region phenomenon in the ionosphere [*Brekke and Rino*, 1978].

[3] Ionospheric Joule heating is an important energy sink for the magnetosphere [*Akasofu*, 1981; *Rodger et al.*, 2001], accounting for ~55–60% of the global energy budget [*Tanskanen et al.*, 2002; *Østgaard et al.*, 2002] and is usually greater than the energy dissipated from particle precipitation [e.g., *Ahn et al.*, 1983; *Banks et al.*, 1977; *Østgaard et al.*, 2002]. Unfortunately, it is difficult to monitor the global ionospheric electric field and Pedersen conductance simultaneously, which is why global Joule heating is often parameterized using geomagnetic indices [e.g., *Aikio and Selkälä*, 2009; *Kosch and Nielsen*, 1995, and references therein]. Height-integrated ionospheric Joule heating is typically <30 mW/m^2, although peak values can be much greater than this [*Kosch and Nielsen*, 1995]. Joule heating is often expressed by the simplified equation, which ignores the neutral wind dynamo:

$$Q_{JH} = E^2 \Sigma\sigma_P \tag{1}$$

where E is the electric field magnitude and $\Sigma\sigma_P$ is the height-integrated Pedersen conductance [*Kosch et al.*, 1998]. The ionospheric Pedersen conductivity is obtained from [*Brekke and Rino*, 1978; *Egeland et al.*, 1973]

$$\sigma_p = \frac{qn_e}{B}\left(\frac{k_e}{1+k_e^2} + \frac{k_i}{1+k_i^2}\right) \tag{2}$$

where q is the electronic charge, n_e is the plasma density from radar measurements, and B is the magnetic field strength. Here $k = \Omega/\nu$, where Ω is the cyclotron frequency, ν the collision frequency with neutrals, and e and i denote electrons and ions, respectively. Also, $\Omega = qB/m$, where m is the species mass. B and ν can be estimated from models. Here σ_P peaks

[1]Solar-Terrestrial Environment Laboratory, Nagoya University, Nagoya, Japan.
[2]Physics Department, Lancaster University, Lancaster, UK.
[3]Department of Physics and Astronomy, University College London, London, UK.
[4]Department of Physics, La Trobe University, Melbourne, Victoria, Australia.
[5]National Institute of Polar Research, Tokyo, Japan.
[6]Space Science and Technology Department, Rutherford Appleton Laboratory, Didcot, UK.
[7]University Centre in Svalbard, Longyearbyen, Norway.

0148-0227/11/2010JA016015

around 120–130 km in the ionosphere. The lower E region ion-neutral collision frequency can be obtained from *Schunk and Nagy* [2009], assuming an ion composition of 75% NO^+ and 25% O_2^+, including resonant collisions between O_2 and O_2^+ [*Schunk and Walker*, 1973], and neglecting lighter ions such as O^+ below 140 km altitude:

$$\nu_i = 4.29 \times 10^{-16} n_{N_2} + 4.23 \times 10^{-16} n_{O_2} + 2.41 \times 10^{-16} n_O \text{ Hz} \quad (3)$$

where n is the neutral density of the relevant species obtained from the MSIS model [*Hedin et al.*, 1977]. Referenced to the fixed frame of the Earth, the ionospheric electric field (E) is expressed by

$$\vec{E} = -\left(\underset{F}{\vec{V}} \times \vec{B}\right) \quad (4)$$

where $\vec{V}_F$ is the ion velocity observed by radar in the near-collisionless F region (>200 km). Assuming no other forces except an electric field in a magnetized plasma, the generalized ion motion (V_i) is given by [*Brekke*, 1997]

$$\underset{i}{\vec{V}} = \frac{k_i}{1+k_i^2}\frac{\vec{E}}{B} + \frac{k_i^2}{1+k_i^2}\frac{\vec{E}\times\vec{B}}{B^2} \quad (5)$$

and the direction of the ion flow relative to the electric field vector (θ) is given by [*Brekke et al.*, 1990]

$$\tan(\theta) = k_i \quad (6)$$

Whether the first or second term of equation (5) dominates the ion velocity direction depends on the value of k_i. In the near-collisionless F layer (>200 km), the second term dominates and the ion velocity is perpendicular to the electric and magnetic field directions. This gives the ionospheric electric field directly from equation (4). In the highly collisional D region (<90 km), the first term dominates and the ion velocity is in the direction of the electric field. However, somewhere in the E region, where $k_i = 1$, the ion flow will be at 45° to the E and $E \times B$ directions. This depends on altitude as Ω_i depends linearly on B and ν_i depends linearly on n_n (see equation (3)). In the auroral zone, for $|E| > 25$ mV/m, *Fujii et al.* [1998] found that ions moved in the $E \times B$ direction at altitudes $\geq$ 117 km and in the E field direction at altitudes $\leq$ 101 km. These altitudes are not fixed since the neutral density (n_n) is variable, as witnessed by strong vertical winds in the E layer up to 50 m/s [e.g., *Price et al.*, 1995] and F layer up to 150 m/s [e.g., *Innis et al.*, 1999; *Rees et al.*, 1984] which are often associated with auroral precipitation or Joule heating events [*Smith*, 1998, and references therein]. Of course, equations (5) and (6) are modified if neutral winds are present as the drag term will add another vector component to the ion velocity, especially below ~110 km [*Brekke et al.*, 1990].

[4] It is well established that high-latitude thermospheric neutral circulation is driven by ion drag, solar heating pressure, advection (momentum), viscous and Coriolis forces. Ion drag through ion-neutral collisions and pressure gradients due to solar heating are normally the dominant driving forces in the F layer [e.g., *Killeen and Roble*, 1984] but advection, solar heating, and Coriolis forces may all exceed the ion drag force, depending on the plasma density height profile [*Crickmore*, 1995]. The pressure from solar heating and the Coriolis force are normally the dominant drivers of neutral dynamics in the E layer although ion drag and advection may also be important depending again on the plasma density [e.g., *Killeen and Roble*, 1984, 1986; *Maeda et al.*, 1999; *Nozawa et al.*, 2005; *Tsuda et al.*, 2007]. *Tsuda et al.* [2009] showed that the pressure gradient from Joule heating could become the dominant force in the E region. In the polar cap, *Nozawa et al.* [2005] and *Tsuda et al.* [2007] showed from ground-based radar observations that ion drag above 118 and 106 km, respectively, played a role in neutral wind acceleration, consistent with >105 km derived from satellite observations by *Richmond et al.* [2003]. On the other hand, *Tsuda et al.* [2007] also showed that ion motion below 104 km in the polar cap was controlled by the neutral winds through collisions. Hence ~105–120 km is the transition region, below which the neutrals control the ions and above which the ions, driven by the magnetospheric convection electric field, control the neutrals.

[5] The ion-neutral coupling e-folding time (τ_{in}) is given by

$$\tau_{in} = \frac{n_n}{n_i}\frac{1}{\nu_i} \text{ s} \quad (7)$$

where n_i is the ion density. In the thermospheric F layer, neutral circulation broadly follows plasma convection with an e-folding time of 0.5–3.5 h [*Heelis et al.*, 2002; *Killeen and Roble*, 1984, 1988; *Kosch et al.*, 2001a], depending on geomagnetic activity, season, and local time. The ion drag e-folding time has not been measured in the E layer. However, since ν_i is linear with n_n (see equation (3)) [*Schunk and Nagy*, 2009], the change in e-folding time essentially becomes a function of plasma density with altitude. At high latitudes, auroral precipitation frequently enhances the E region plasma density by an order of magnitude or more, enhancing coupling between ions and neutrals. Therefore the dominant circulation driver, i.e., ions or neutrals, depends on the local plasma density [*Tsuda et al.*, 2007].

[6] E region winds maximize around 100–110 km altitude with maximum speeds exceeding 100 m/s [*Nozawa and Brekke*, 1999] and may experience a large shear with a vertical scale of 10 km or less [*Larsen*, 2002]. The E region neutral wind (U_E) can be derived from radar observations of the E region ion velocity (V_E) as follows [*Rino et al.*, 1977]:

$$\underset{E}{\vec{U}} = \underset{E}{\vec{V}} - \frac{k_i}{B}\left(\vec{E} + \underset{E}{\vec{V}} \times \vec{B}\right) \quad (8)$$

where E is obtained from equation (4). This has been done successfully in the height range 90–120 km using a model for ν_i to obtain k_i [e.g., *Maeda et al.*, 1999; *Nozawa and Brekke*, 1999; *Nozawa et al.*, 2005, 2006; *Tsuda et al.*, 2007]. If the assumption $U_E = 0$ is made, then equation (8) can be trivially rearranged to solve for k_i and hence ν_i. This has been done successfully for heights <140 km [e.g., *Davies et al.*, 1997, and references therein]. However, if U_E is also observed by an optical method (described below) then ν_i can be determined uniquely without any assumptions. A similar technique has been used in the F region using radar and optical observations at high [*Winser et al.*, 1988; *Davis et al.*, 1995] and low [*Burnside et al.*, 1987] latitudes. We employ this ground-based

technique for the first time in the lower E region using simultaneous ion and neutral flow observations. Once ν_i is known, equation (3) is trivially rearranged to solve for n_n, although it is not possible to determine the neutral composition. The solar minimum period of cycle 23/24 recently ended has experienced solar and geomagnetic activity at their lowest point for a century [*Lockwood et al.*, 2009; *Russell et al.*, 2010]. Deep solar minima are associated with atmospheric cooling and therefore contraction [*Emmert et al.*, 2010; *Russell et al.*, 2010]. Satellite observations of the ionosphere [e.g., *Heelis et al.*, 2009] and the thermosphere [e.g., *Emmert et al.*, 2010] at 400 km altitude show that both were cooler and less dense in 2008 than at any other time since the beginning of the space age. In particular, *Emmert et al.* [2010] found that the global average thermospheric mass density to be 10–30% lower than expected. Since estimates of anthropogenic forcing and long-term climatological trends cannot account for most of the density change [*Emmert et al.*, 2010], the main driver appears to be solar EUV [*Solomon et al.*, 2010]. We use equations (8) and (3) to compare the E region ion-neutral collision frequency from observations to that derived from the MSIS atmospheric model.

[7] Thermospheric neutral winds and temperatures can be derived from passive Doppler measurements of the naturally occurring 630 and 557.7 nm optical emissions in the F and E layers, respectively, using ground-based Fabry-Perot interferometers (FPI) [e.g., *Hernandez*, 1986]. Since these are passive observations, the derived neutral winds and temperatures will be an average in altitude weighted according to the optical emission intensity profile. Traditionally, an average neutral wind vector has been derived by scanning the sky at different azimuths at a fixed zenith angle for an assumed altitude, typically close to ~240 and ~115 km for 630 and 557.7 nm, respectively [*Griffin et al.*, 2006; *Kosch et al.*, 2000a]. This technique is greatly enhanced by the recent development of scanning Doppler imagers (SDI), which can derive line-of-sight wind measurements from many tens of software-defined directions simultaneously in a wide field of view [*Conde and Smith*, 1997, 1998]. The information from all line-of-sight Doppler measurements is used to derive an equivalent horizontal wind vector field assuming the vertical winds are small. Details of the fitting algorithm are given by *Anderson et al.* [2009, and references therein]. The assumption of small vertical thermospheric winds, especially in the E region, is generally valid for quiet to moderate geomagnetic conditions [e.g., *Kosch et al.*, 2000b]. In addition, a practical difficulty is that the SDI can only unambiguously measure vertical winds in the zenith line of sight and it cannot be assumed that this vertical atmospheric motion is the same over the whole instrument's field of view [e.g., *Price et al.*, 1995; *Kosch et al.*, 2000b]. Despite this limitation, the SDI is powerful for two reasons: (1) it can differentiate between spatial and temporal ambiguities in the thermospheric neutral wind field and (2) it observes with mesoscale resolution in multiple directions simultaneously. The typical time resolution of this optical technique is 1–20 min, depending on the emission intensity. The typical spatial resolution is about 50 and 100 km in the E and F layers, respectively.

[8] The O^1S emission at 557.7 nm results from a combination of three sources, namely, airglow around the mesopause at about 97 km [*Phillips et al.*, 1994], dissociative recombination in the thermosphere, and auroral particle precipitation in the E region [*Rees*, 1989]. The primary flux of electron energy into the auroral atmosphere is 1–10 keV [*Burch*, 1991]. Optical triangulation has shown that the aurora normally occurs above 100 km altitude [*Currie*, 1955; *Störmer*, 1955]. At high latitudes, the auroral component dominates when present but can be highly variable in intensity and height, which is related to the energy (Y) of the precipitating particles as follows [*del Pozo et al.*, 1997]:

$$Y(H) = 4 \times 10^5 e^{-0.101H} (\text{keV}) \tag{9}$$

where H is height in kilometers. Since the O^1S emission may occur at any height from ~97 to ~200 km, spanning many scale heights, no default altitude can be assumed when making passive observations. However, the altitude can be determined either by comparing the observed neutral and ion temperatures derived from SDI and radar data, respectively, comparing the observed neutral temperature with thermospheric models (e.g., CTIP) [*Kosch et al.*, 2010] or by modeling the photon production rate from the plasma density profile [*Link and Cogger*, 1988; *Vlasov et al.*, 2005]. In the lower E region, $T_i \approx T_n$ to a reasonably good approximation [*Griffin et al.*, 2006; *Kurihara et al.*, 2009; *Nozawa et al.*, 2006]. During periods of Joule heating, $T_i > T_n$ by up to ~20% have been inferred from radar data between 105 and 115 km altitude [*Maeda et al.*, 2002]. During periods of large electric field enhancements (100 mV/m) T_i can exceed T_n by up to ~30% at 116 km [*Maeda et al.*, 2005, Figure 3]. In this study we have used the last two methods for estimating the effective 557.7 nm emission height.

[9] The spatial scales of structures in the ionospheric auroral plasma can vary from the whole auroral oval down to the Debye length limit [*Galperin*, 2002]. In particular, auroral arcs may be 100s to even 1000s of km geomagnetic east-west aligned but the average optical width of steady state auroral arcs is only 18 ± 9 km [*Knudsen et al.*, 2001]. Auroral precipitation is associated with upward FACs [e.g., *Arnoldy*, 1974; *Kamide and Akasofu*, 1976] and local changes in ionospheric conductivity [e.g., *Kosch et al.*, 2001b]. The upward FAC must return via an equivalent downward FAC in order to satisfy current continuity, connecting in the ionosphere via Pedersen currents [*Tsunoda et al.*, 1976] and dissipating energy in the form of Joule heating (see equation (1)). The closing downward current normally appears equatorward (poleward) of the auroral arc in the dusk (dawn) sector, consistent with the large-scale ionospheric electric field associated with ionospheric convection [*Aikio et al.*, 1993; *Armstrong et al.*, 1975; *Lewis et al.*, 1994], although this is not always the case [*Opgenoorth et al.*, 1990]. Normally, the local arc-induced ionospheric electric field enhances the large-scale convection electric field. However, the downward current is carried by cold ionospheric electrons propagating upward [*Arnoldy*, 1974], which leaves a region typically less than 100 km wide adjacent to the auroral arc where a plasma depletion of 20 to 70% (average 45%) may occur within a minute, though it typically takes 5 min to develop [*Doe et al.*, 1993, 1995]. The plasma depletion results in a similar decrease in Pedersen conductivity (see equation (2)). Hence in order to satisfy current continuity, intense horizontal ionospheric electric fields, possibly exceeding 100 mV/m, pointing into the auroral arc can develop in a narrow region, possibly less than 45 km wide, on the equatorward (poleward)

side of auroral arcs in the dusk (dawn) sector [*Aikio et al.*, 1993; *Fujii et al.*, 2009; *Lewis et al.*, 1994; *Opgenoorth et al.*, 1990]. Radar [e.g., *McCrea et al.*, 1991; *Stiles et al.*, 1980] and rocket studies [e.g., *Evans et al.*, 1977; *Marklund et al.*, 1982] have all found that strong Joule heating occurred near the boundaries of auroral arcs but was weak within the aurora itself.

[10] *Codrescu et al.* [1995] showed that including electric field variability always increased the estimated Joule heating rate compared to using averaged electric fields. Using temporally and spatially averaged electric fields can result in 20–65% [*Rodger et al.*, 2001] and 50% [*Codrescu et al.*, 2000] underestimation of the total Joule heating, respectively. In addition, *Cierpka et al.* [2000] showed that ignoring the *F* region neutral wind when estimating the ionospheric electric field resulted in an error of up to 60% in the *F* layer Joule heating calculation. *Aruliah et al.* [2004] found that the *F* region neutral wind dynamo was on average 50% of the magnetospheric electric field and contributed an average 41% of in situ Joule heating. A similar study has not been done in the *E* layer, although *Brekke and Rino* [1978] found the maximum in ionospheric Joule heating occurred around 110–130 km altitude. Of course, the *E* region neutral winds can substantially affect the transfer of energy from the magnetosphere into the ionosphere. *Fujii et al.* [1999] and *Thayer* [1998] estimated that ~35% and ~30%, respectively, of the total energy entering the ionosphere went into accelerating the *E* region neutral wind and the rest into Joule heating. However, the *E* region neutral wind effect is height dependent and the neutral winds can also act as a dynamo releasing energy into the thermosphere [*Fujii et al.*, 1999; *Thayer*, 1998]. *Kosch et al.* [2010] showed that mesoscale neutral winds in the upper *E* region (>128 km) could be dramatically changed by the appearance of auroral arcs. They showed that the neutral winds within ~50 km of an auroral arc could rotate their direction by ~90° within 7–16 min in the height range ~130–200 km. This was attributed to ion drag as a result of the enhanced electric field and plasma density associated with auroral precipitation, which is consistent with *Nozawa et al.* [2005] who found that ion drag became an important force above 107 and 118 km in the auroral oval and polar cap, respectively.

[11] The Coupled Thermosphere Ionosphere Plasmasphere (CTIP) model [*Fuller-Rowell and Rees*, 1980; *Millward et al.*, 1996] consists of a global thermospheric model, a high-latitude ionospheric model, and a midlatitude and low-latitude ionosphere/plasmasphere model. The thermospheric code simulates the time-dependent global structure of the wind vector, temperature, and density of the neutral thermosphere by numerically solving the nonlinear equations of momentum, energy, and continuity on a 3-D spherical polar grid rotating with the Earth. The high-latitude ionosphere convection model calculates field-aligned ion velocity components from the field-aligned momentum equation. The model includes chemistry, gravity, and ion-ion and ion-neutral collisional drag. The ionosphere is computed self-consistently with the thermosphere poleward of 23° latitude in both hemispheres. Transport under the influence of magnetospheric electric fields is explicitly treated, assuming $E \times B$ drifts and collisions with neutral particles. CTIP uses the following input parameters: Hemispheric Power (GW) and Hemispheric Power index (activity level), F10.7 radio flux, and ionospheric electric fields obtained from the Weimar electrodynamics model which uses solar wind density and velocity as well as IMF data for input. The model latitude, longitude, and time resolution is 2°, 18°, and 72 min, respectively, and the altitude range spans approximately 80 to 1000 km in 15 logarithmically spaced pressure levels. *Codrescu et al.* [1997] found that a closely related model (CTIM) underestimated the global large-scale thermospheric neutral temperature compared to measurements during geomagnetic storms when the average electric field was used for Joule heating calculations. However, it is clear that the reason for this discrepancy is because the CTIP/CTIM model neither has the spatial nor temporal resolution to directly model mesoscale auroral features. This is true for all current atmospheric general circulation models.

[12] The strength of the FAC, ionospheric Joule heating, plasma convection, and neutral winds are all increased during geomagnetic activity and auroral substorms and never disappear completely even during quiet periods [e.g., *Aruliah et al.*, 1991; *Kosch and Nielsen*, 1995, 2001; *McCormac et al.*, 1987; *Senior et al.*, 1990]. It is clear that mesoscale observations of the ionospheric electric field and Pedersen conductance as well as the thermospheric neutral winds are important to the total global energy budget of the magnetosphere-thermosphere system. In the past, such spatial resolution has not normally been available over a wide field of view. We present mesoscale spatial observations of *E* region Joule heating in the vicinity of an auroral arc with unprecedented spatial resolution.

2. Experiment and Data

[13] Simultaneous *E* region observations of neutral wind and ion flow in the vicinity of an auroral arc have been undertaken using a Scanning Doppler Imager (SCANDI) [*Aruliah et al.*, 2010] and the EISCAT Svalbard Radar (ESR) [*Wannberg et al.*, 1997], both located at 78.2° N, 16.0° E in the polar cap near Longyearbyen on Svalbard. SCANDI observed 557.7 nm in the *E* region with 7 min integration. Figure 1 shows the data layout of SCANDI (black solid lines) in an all-sky angular format. The field of view is subdivided into 25 sectors within four azimuthal annuli with zenith angles of 0–16° (1 sector), 17–44° (4 sectors), 45–59° (8 sectors), and 60–67° (12 sectors). This corresponds to horizontal radial distances at the center of each annulus of 0, 62, 140, and 218 km at an altitude of 110 km. The colocated traditional FPI was intended to observe 630.0 nm in the *F* region by pointing in the four cardinal directions plus vertical but a technical fault resulted in 557.7 nm observations only from this instrument. We therefore have no *F* region neutral wind observations.

[14] It was intended that the ESR 32 m dish scan 360° in azimuth angle at 1.5°/s with a constant zenith angle in the middle of each SCANDI annulus, i.e., at 30, 52, and 64° zenith angle. The intended dish scan sequence was 360° clockwise at 30° zenith angle, 360° anticlockwise at 52° zenith angle, 360° clockwise at 64° zenith angle, 360° anticlockwise at 52° zenith angle, repeated continuously. ESR license restrictions did not permit the 64° zenith angle, so the maximum zenith angle allowed was used (60°). To prevent cable wind-up because of the odd number of SCANDI annuli, the middle annulus was scanned twice in each cycle. During zenith angle changes, set for azimuth = 135°, the transmitter was to be

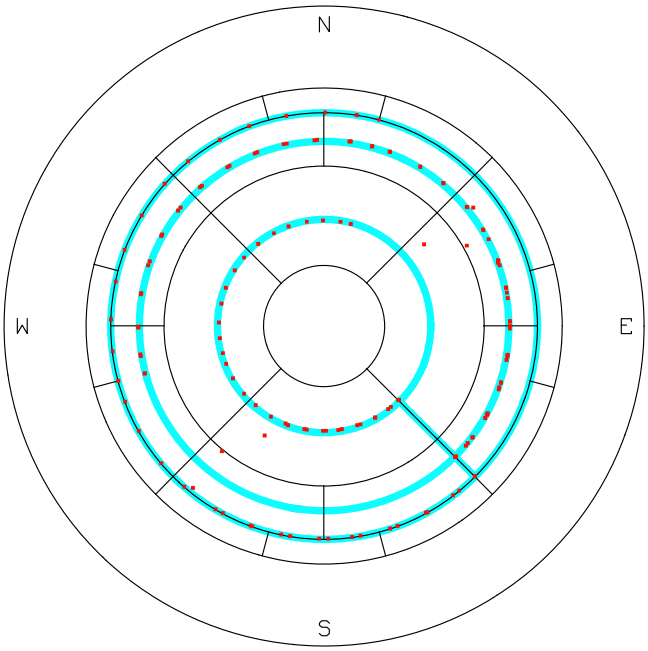

Figure 1. SCANDI sectors (black), intended ESR scan (blue), and actual ESR data points (red) on an all-sky projection. The outer circle represents the horizon at a zenith angle of 90°.

connected to the fixed field-aligned 42 m dish to make near-vertical observations (field-aligned at 8°S). The intended ESR 32 m dish scan is shown in Figure 1 (blue lines). The ESR was operated using the standard STEFFE1 radar code with range gates from 90 to 1000 km, a range resolution of 2.4 km and 6.4 s data integration time. Unfortunately, a synchronization error of the azimuth and zenith control of the 32 m dish, as well as the transmitter switching times to the 42 m dish, occurred. Figure 1 shows the ESR measurement locations in 6.4 s increments for a complete scan (red squares). Multiple data from the same position are not obvious where the dish was stationary, especially for the middle annulus. The net result was that the 32 m dish spent too much time at azimuth = 135° making multiple observations without changing zenith angles or switching the transmitter to the 42 m dish, zenith angle changes took place at incorrect azimuth angles, and switching the transmitter to the 42 m dish resulted in large data gaps in the 32 m azimuth scan (approximately one third of each azimuth scan is missing data). To ameliorate the situation, the two highest zenith angle scans have been combined, effectively eliminating all ESR data gaps for the middle SCANDI annulus. The effective zenith angle for this synthesized ESR annulus is 56° with the original data corrected for the geometry change. The highest zenith angle SCANDI data effectively has no ESR data to accompany it, thereby reducing the field of view of this study. For the low zenith angle ESR scan, the missing data have been modeled using the vector fitting algorithm [*Anderson et al.*, 2009]. Of the total 17.8 min radar scan time, 4 min is spent on the 30° zenith angle, 12 min is spent on the synthesized 56° zenith angle, and 1.8 min is spent changing zenith angle or not scanning. Of course, the 42 m dish field-aligned data were unaffected.

[15] Horizontal ion flow fields have been derived from the line-of-sight ion velocity data using a similar algorithm to that used to derive the neutral wind fields. This algorithm is described in detail by *Anderson et al.* [2009, and references therein] and is routinely used to generate neutral wind vector fields. However, for the ion flow fields the algorithm has been modified to allow for the uneven azimuth sampling resulting from the dish scan error. Instead of directly calculating the Fourier coefficients around each azimuthal ring (as is done for the neutrals), these coefficients have been obtained by least squares fitting a sinusoidal function to the azimuthal variation of line-of-sight velocity data in each annulus. Each component of the flow field is then described by a first-order Taylor expansion about the zenith, with uniform flow and gradient terms given in terms of the fitted Fourier coefficients. As with the neutrals, the assumption of a constant magnetic meridional flow field along the magnetic zonal direction has been used to constrain the fit. Note that the resulting vector flow fields (neutrals and ions) make use only of the fitted component normal to the line of sight when line-of-sight data is available at a given position in the sky; thus each fitted vector is made up of a directly measured line-of-sight component and a fitted normal component, and the derived vector flow fields retain any mesoscale variability present in the measured line-of-sight data.

[16] A significant limitation of the ESR scan is that it took 17.8 min to complete. This is approximately 2.5× longer than the SCANDI integration (7 min). Therefore it was necessary to find an aurora that was stationary within the field of view for this length of time. This scenario only occurred approximately once within the 3 day campaign covering 2, 9, and 16 February 2010. We analyze an almost-stationary aurora for 2336–2354 UT on 2 February 2010. We also investigate geomagnetically quiet periods before (2312–2330 UT on 2 February 2010) and after (0036–0054 UT on 3 February 2010, hereafter labeled 2436–2454 UT) the aurora appeared. Here 2312–2330 UT had no aurora present and 2436–2454 UT had some quiet aurora present near the southeast horizon. All periods are used for mesoscale Joule heating calculations. Only the last period is used for estimating the *E* region ion-neutral collision frequency using equation (8). Geomagnetic conditions were moderately active with K_p = 3–4 in the period of interest. The IMF data from the ACE satellite in GSM coordinates, adjusted by 48 min to account for the solar wind speed of ~520 km/s, gives B_z in the range −5.9 to +2.8 nT, B_y in the range −2.2 to −6.0 nT and B_x in the range +0.1 to +4.6 nT throughout the period of interest. SuperDARN global ionospheric convection (not shown) shows Longyearbyen under a weakly developed dawn convection cell, consistent with B_z mostly positive and B_y negative. There are no SuperDARN backscatter data directly over Longyearbyen; however, weak eastward convection is observed over the northern Scandinavian sector.

[17] Inverting the plasma density profiles obtained from the ESR field-aligned 42 m dish gave the effective 557.7 nm emission altitude to be in the range 105–117 km with an average of 110.5 km during the periods of interest [*Link and Cogger*, 1988; *Vlasov et al.*, 2005]. From equation (9), this is consistent with auroral precipitation of 3–10 keV [*del Pozo et al.*, 1997]. The CTIP model has low temporal resolution (72 min.) but comparing modeled and observed neutral

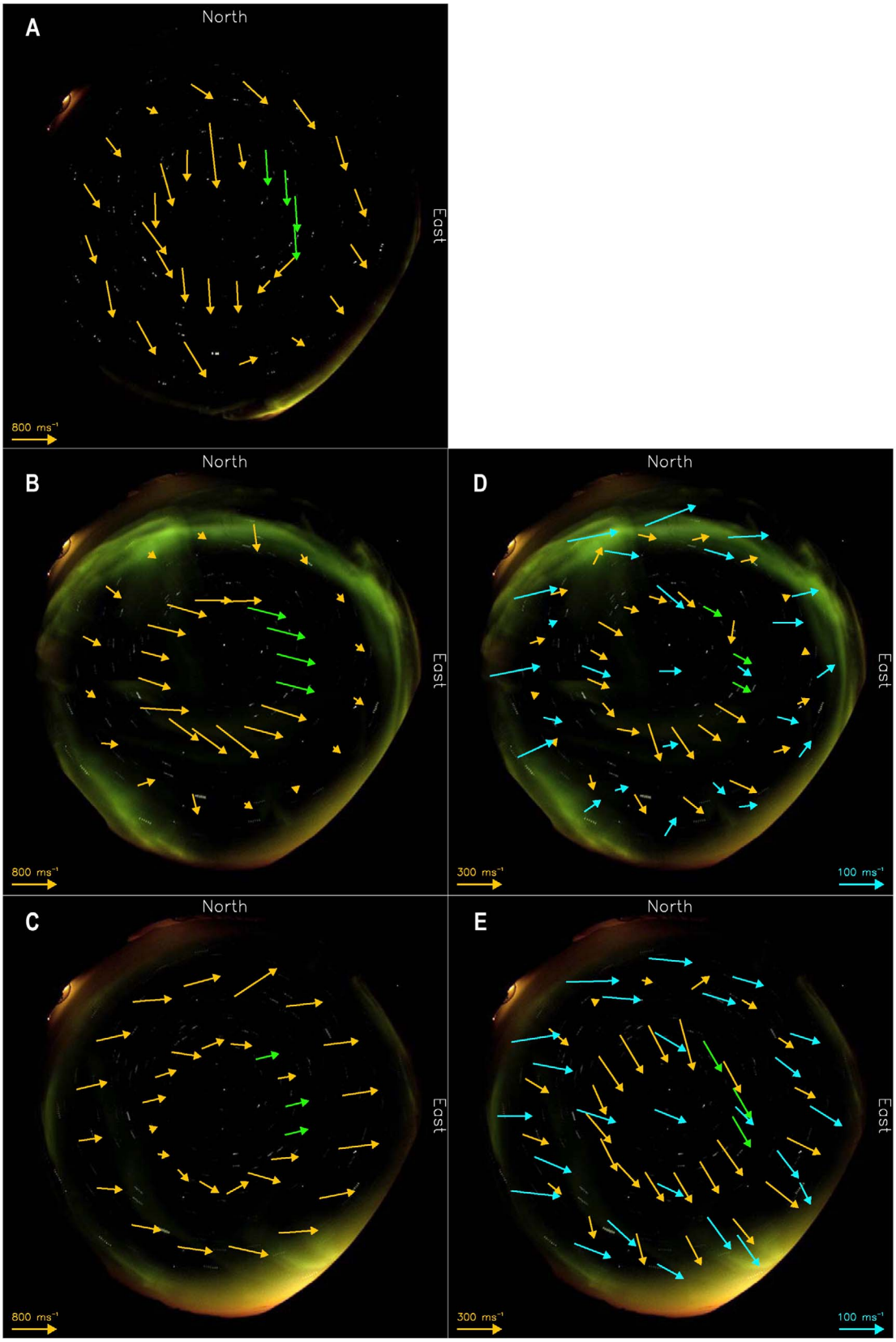

Figure 2. Averaged all-sky images of the aurora with *F* region ion (yellow) flow vectors overlaid for (a) 2312–2330 UT, (b) 2336–2354 UT, (c) 2436–2454 UT and with *E* region ion (yellow) and neutral (blue) flow vectors overlaid for (d) 2336–2354 UT and (e) 2436–2454 UT on 2 February 2010. The green vectors are modeled without line-of-sight data.

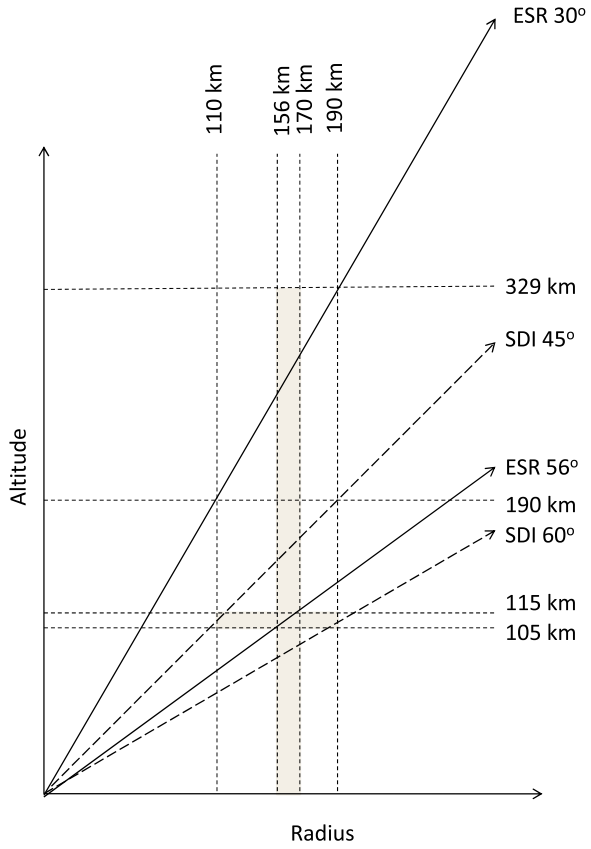

Figure 3. A schematic vertical cut radially through the ESR scan space. The plot is approximately to scale. The ESR beam directions are represented by solid arrows. The SCANDI sector boundaries are represented by dashed arrows. Angles are measured in degrees from the zenith.

temperatures (~360 K) at 2340 UT gives a height of ~114.5 km, consistent with the estimate (~109.3 km) based on the ESR data for the same time. The ESR 32 m data was binned into 22.5° azimuthal sectors and height integrated for 105–115 km in the *E* region and 200–300 km in the *F* region, the latter primarily to obtain the ionospheric electric field. Unfortunately, the nighttime *E* region plasma density in the polar cap during solar minimum was so low in the absence of aurora ($<2 \times 10^{10}$ el/m^3) that the radar observations have low signal-to-noise ratio. However, expanding the *E* region height range beyond one scale height (~10 km) was considered undesirable. Increasing the integration time is not possible because of the continuous 32 m dish motion. However, when the aurora appeared the plasma density was $\geq 5 \times 10^{10}$ el/m^3. The situation in the *F* layer is significantly better because of the higher plasma density and 100 km height integration. Hence we are unable to use the *E* region ion temperature data to provide an accurate cross-check of the 557.7 nm emission altitude estimate. The *E* region neutral temperature, averaged over the entire field of view, is ~375–415 ± 5 K during the period of interest and is consistent with the ion temperature in the same height range. Our observations agree well with previous ESR ion temperature observations [*Maeda et al.*, 2002, 2005] obtained without beam scanning and employing longer integration times. The low neutral temperature variability indicates a relatively constant 557.7 nm emission altitude. The ESR plasma density and velocity observations were usable throughout the experiment. During the periods of interest, the field-aligned ion velocity was < 65 m/s while the vertical *E* region neutral wind was < 20 m/s. Therefore along with the almost-stationary aurora, the conditions for obtaining the equivalent horizontal ion flow in the *E* and *F* regions, and neutral flow in the *E* region, were reasonably met.

[18] Figure 2 shows the fitted horizontal ESR ion velocities (yellow) and SCANDI neutral velocities (blue) overlaid on an averaged all-sky image in geographic coordinates. The green vectors at low zenith angle are modeled data to close the ESR data gaps (described above). Each vector is centered on its location. Note the different vector scales for each data type. Figures 2a, 2b, and 2c show the spatial distribution of *F* region ion flow in 22.5° sectors for 30 and 56° zenith angle at 2312–2330, 2336–2354, and 2436–2454 UT, respectively. Figures 2d and 2e show the spatial distribution of *E* region ion flow in 22.5° sectors for 30 and 56° zenith angle at 2336–2354 and 2436–2454 UT, respectively, for 105–115 km altitude. Overlaid are the *E* region neutral wind vectors, one for each SCANDI sector. The *E* region ion and neutral flow data for 2312–2330 UT are not shown because of the low plasma density and optical emission intensity from the lack of particle precipitation, which resulted in low ESR and SCANDI data signal-to-noise ratios. An unfiltered all-sky color camera recorded optical images of the sky every 3 min using 2 min integration. The arithmetic mean of the appropriate images was taken to form a single image for each of the three selected study periods (each of ~18 min duration) to demonstrate that the aurora is either absent or present and near stationary. The white dotted arcs in the images are due to the moving stars. The yellow illumination on the northwest horizon is stray light from a neighboring instrument dome. Note that the figures are in angular coordinates, so the *F* layer data does not overlay the *E* layer data directly. Likewise, the location of the *F* region ion flow vectors does not relate well to that of the aurora.

[19] The geometry of the experiment has the low zenith angle annulus in the *F* region vertically above the high zenith angle annulus in the *E* region, which coincides with the middle annulus of *E* region neutral winds from SCANDI. The magnetic field inclination over Svalbard is only ~8°, i.e., effectively vertical. Figure 3 shows a schematic vertical cut radially through the data presented in Figure 2. The figure is approximately to scale. The ESR beam directions are represented by solid arrows at 30° and 56° zenith angle. The SCANDI sector boundaries are represented by dashed arrows at 45° and 60° zenith angle. For the height range 105–115 km, the synthesized *E* region ESR data at 56° zenith angle covers a radial distance of 156–170 km, whereas the SCANDI sector at 45–60° zenith angle covers 110–190 km. We denote the effective radial distance of the combined data as 163 km. This gives an azimuthal distance of 64 km for the 22.5° sectors. The *F* region ESR data at 30° zenith angle intersects the middle annulus SCANDI sector boundaries at 190–329 km altitude, which conveniently allows integration over 200–300 km in the *F* layer to obtain a good estimate of the ionospheric electric field from equation (4). Unfortunately, the *F* region neutral winds are unknown. However, since we

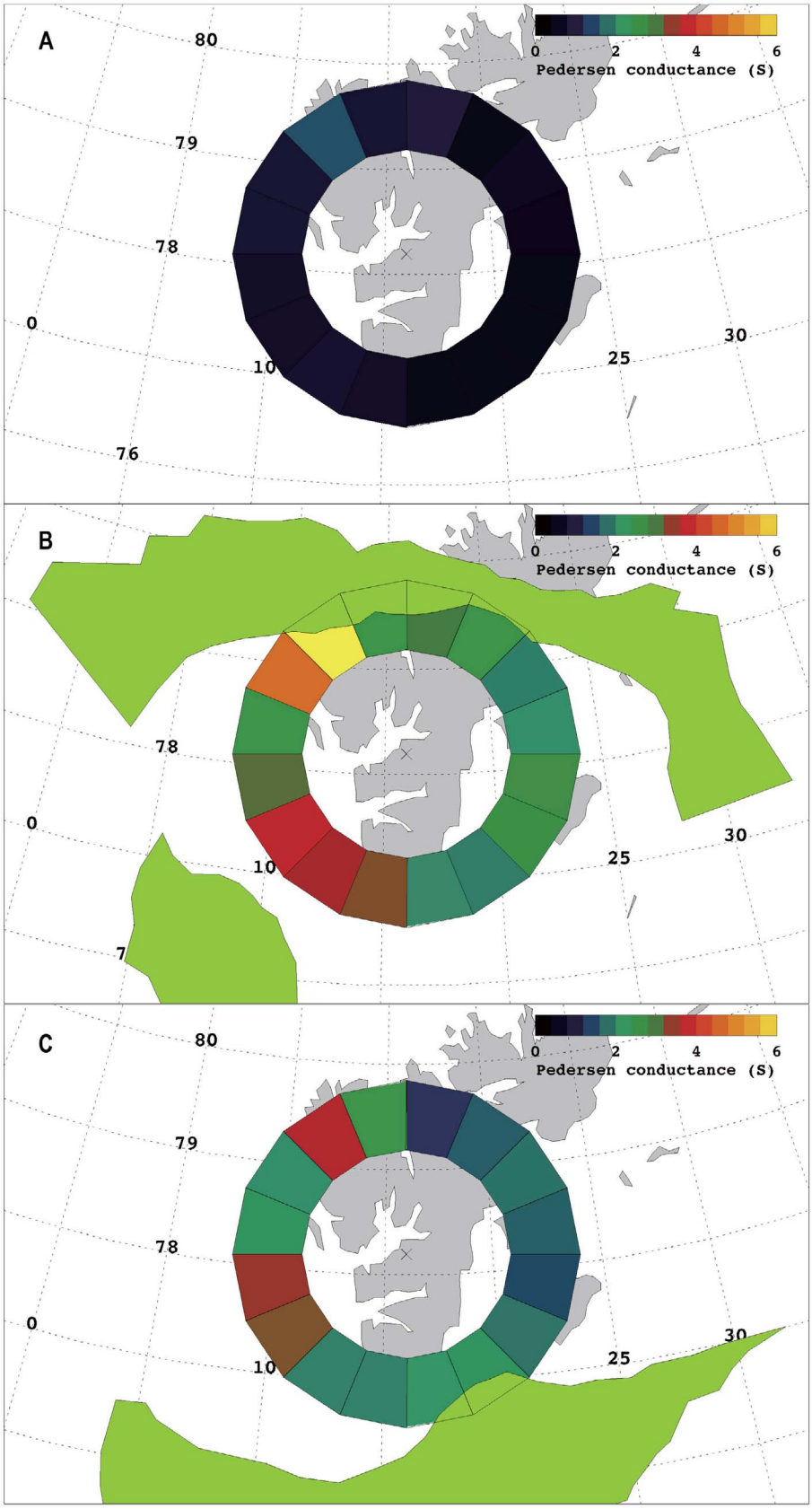

Figure 4. The spatial distribution of Pedersen conductance in 22.5° sectors about Longyearbyen projected to 110 km for (a) 2312–2330 UT, (b) 2336–2354 UT, and (c) 2436–2454 UT on 2 February 2010. In Figures 4b and 4c the aurora is overlaid for 110 km altitude.

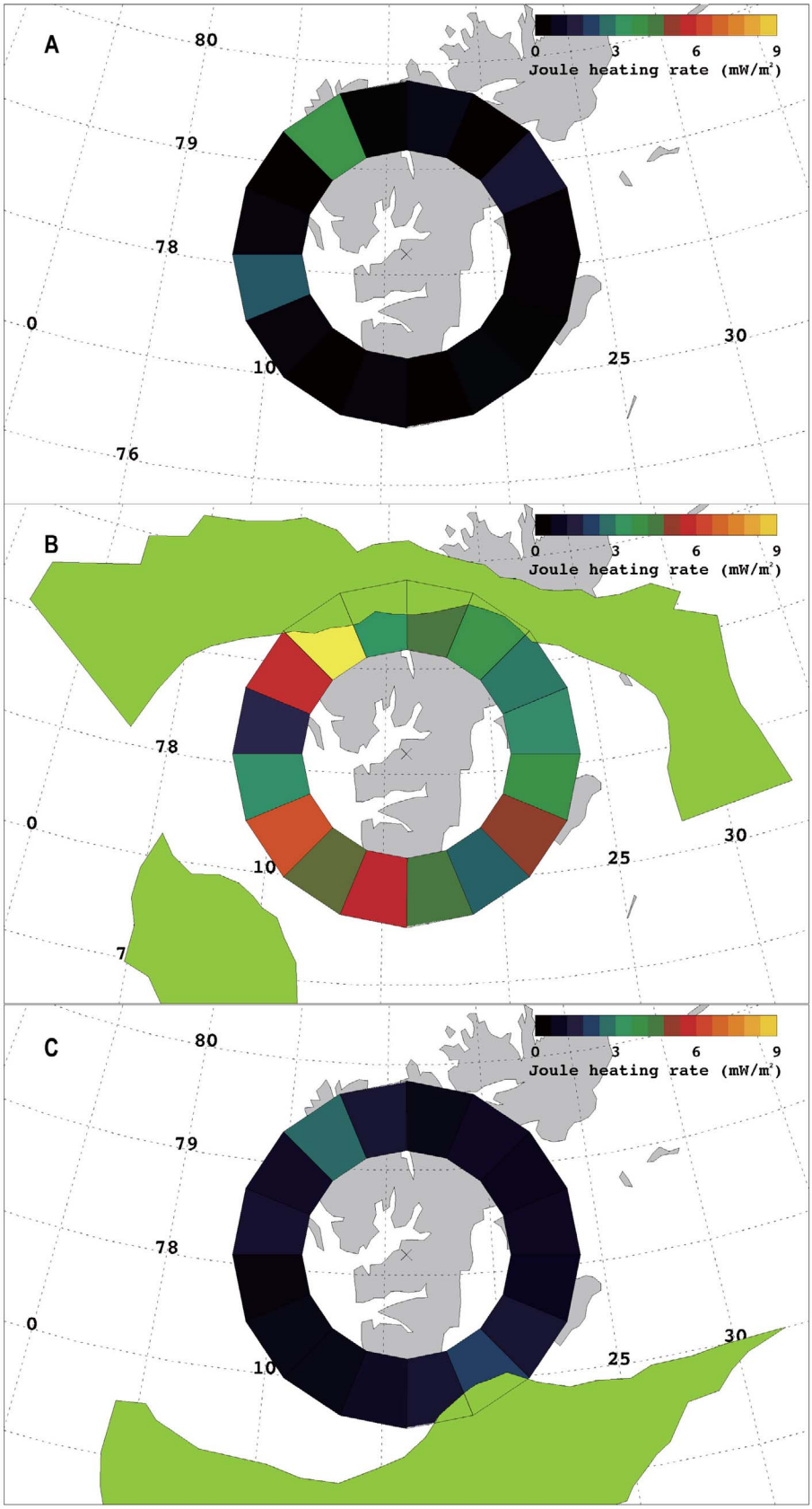

Figure 5. The spatial distribution of Joule heating in 22.5° sectors about Longyearbyen projected to 110 km for (a) 2312–2330 UT, (b) 2336–2354 UT, and (c) 2436–2454 UT on 2 February 2010. In Figures 5b and 5c the aurora is overlaid for 110 km altitude.

Table 1. Pedersen Conductance (C, mho), Integrated Between 95 and 145 km Altitude, Ionospheric Electric Field (E, mV/m), Joule Heating Values (J, mW/m^2) for the Middle SCANDI Annulus Along With Error Estimates[a]

Sector and Azimuth Range		2312–2330 UT	2336–2354 UT	2436–2456 UT
360° Average	C	0.52 ± 0.04	2.79 ± 0.06	1.98 ± 0.06
	E	32.6 ± 7.2	38.1 ± 6.5	19.8 ± 3.8
	J	0.63 ± 0.22	4.1 ± 1.4	0.81 ± 0.31
	T_n		393 ± 2.6	381 ± 3.0
Sector 1 0°–22.5°	C	0.79 ± 0.15	2.77 ± 0.08	1.09 ± 0.03
	E	21.5 ± 4.7	39.2 ± 6.7	19.0 ± 3.6
	J	0.36 ± 0.17	4.24 ± 1.5	0.39 ± 0.15
	T_n		386 ± 1.8	392 ± 3.1
Sector 2 22.5°–45.0°	C	0.24 ± 0.01	2.21 ± 0.03	1.46 ± 0.07
	E	33.4 ± 7.4	38.2 ± 6.5	21.1 ± 4.0
	J	0.27 ± 0.12	3.2 ± 1.1	0.65 ± 0.25
	T_n		386 ± 1.8	392 ± 3.1
Sector 3 45.0°–67.5°	C	0.43 ± 0.03	1.73 ± 0.07	1.65 ± 0.11
	E	33.4 ± 7.4	38.2 ± 6.5	16.1 ± 3.1
	J	0.48 ± 0.22	2.5 ± 0.9	0.43 ± 0.16
	T_n		445 ± 2.7	419 ± 2.9
Sector 4 67.5°–90.0°	C	0.34 ± 0.01	1.87 ± 0.02	1.48 ± 0.02
	E	33.4 ± 7.4	38.2 ± 6.5	21.1 ± 4.0
	J	0.81 ± 0.38	2.7 ± 0.9	0.66 ± 0.25
	T_n		445 ± 2.7	419 ± 2.9
Sector 5 90.0°–112.5°	C	0.27 ± 0.01	2.43 ± 0.02	1.27 ± 0.02
	E	33.4 ± 7.4	38.2 ± 6.5	21.1 ± 4.0
	J	0.30 ± 0.13	3.5 ± 1.2	0.56 ± 0.21
	T_n		437 ± 3.4	417 ± 2.9
Sector 6 112.5°–135.0°	C	0.24 ± 0.02	2.41 ± 0.02	1.66 ± 0.02
	E	26.6 ± 5.9	44.6 ± 7.6	24.5 ± 4.7
	J	0.17 ± 0.08	4.8 ± 1.6	1.0 ± 0.38
	T_n		436 ± 3.4	417 ± 2.9
Sector 7 135.0°–157.5°	C	0.27 ± 0.01	1.71 ± 0.02	1.98 ± 0.02
	E	22.0 ± 4.8	36.3 ± 6.2	30.1 ± 5.7
	J	0.18 ± 0.06	2.26 ± 0.77	1.79 ± 0.68
	T_n		386 ± 2.5	379 ± 2.8
Sector 8 157.5°–180.0°	C	0.24 ± 0.01	1.79 ± 0.02	1.92 ± 0.05
	E	30.4 ± 6.7	48.5 ± 8.35	22.3 ± 4.2
	J	0.22 ± 0.10	4.2 ± 1.4	0.95 ± 0.36
	T_n		386 ± 2.	379 ± 2.8
Sector 9 180.0°–202.5°	C	0.50 ± 0.07	3.13 ± 0.02	1.75 ± 0.02
	E	30.7 ± 6.8	40.5 ± 6.9	19.8 ± 3.8
	J	0.47 ± 0.22	5.1 ± 1.7	0.68 ± 0.26
	T_n		370 ± 2.5	343 ± 2.7
Sector 10 202.5°–225.0°	C	0.60 ± 0.02	3.30 ± 0.04	1.76 ± 0.05
	E	28.1 ± 6.2	36.5 ± 6.2	14.2 ± 2.7
	J	0.47 ± 0.21	4.4 ± 1.5	0.35 ± 0.14
	T_n		370 ± 2.5	343 ± 2.7
Sector 11 225.0°–247.5°	C	0.52 ± 0.08	3.40 ± 0.04	3.10 ± 0.05
	E	28.2 ± 6.2	43.0 ± 7.3	10.3 ± 2.0
	J	0.41 ± 0.19	6.3 ± 2.1	0.33 ± 0.13
	T_n		384 ± 3.1	349 ± 3.2
Sector 12 247.5°–270.0°	C	0.54 ± 0.03	2.91 ± 0.11	3.24 ± 0.04
	E	35.6 ± 7.8	31.1 ± 5.3	7.4 ± 1.4
	J	0.68 ± 0.30	2.8 ± 1.0	0.18 ± 0.07
	T_n		384 ± 3.1	349 ± 3.2
Sector 13 270.0°–292.5°	C	0.65 ± 0.06	2.14 ± 0.03	2.0 ± 0.04
	E	34.3 ± 7.6	25.7 ± 4.4	21.2 ± 4.0
	J	0.76 ± 0.34	1.42 ± 0.48	0.90 ± 0.34
	T_n		375 ± 2.8	363 ± 3.5
Sector 14 292.5°–315.0°	C	0.68 ± 0.06	4.51 ± 0.18	1.87 ± 0.03
	E	42.3 ± 9.3	35.0 ± 6.0	19.7 ± 3.8
	J	1.21 ± 0.55	5.5 ± 1.9	0.73 ± 0.28
	T_n		375 ± 2.8	363 ± 3.5
Sector 15 315.0°–337.5°	C	1.33 ± 0.03	6.16 ± 0.14	3.36 ± 0.13
	E	29.2 ± 6.4	40.3 ± 6.9	26.5 ± 5.0
	J	1.14 ± 0.50	10.0 ± 3.4	2.4 ± 0.9
	T_n		365 ± 1.8	385 ± 3.2
Sector 16 337.5°–360.0°	C	0.62 ± 0.08	2.24 ± 0.04	2.15 ± 0.19
	E	58.5 ± 12.9	36.4 ± 6.2	21.5 ± 4.1
	J	2.11 ± 0.10	3.0 ± 1.0	1.0 ± 0.39
	T_n		364 ± 1.8	385 ± 3.2
Maximum percentage variation	C	210%	51%	115%
	E	114%	60%	115%
	J	308%	90%	269%
	T_n		22.0%	22.0%

[a]For each time period, the average, individual sector values, and uncertainties are given along with the maximum percentage variation. For 2336–2354 UT, sectors 1–3, 10–11, and 14–16 are excluded from the maximum percentage variation calculation in order to exclude the aurora. Note that the neutral temperature (T_n) is measured in 45° sectors and is omitted for the first time period because the 557.7 nm emission altitude was at the mesopause altitude (97 km).

use the Earth as our frame of reference, this omission is of no practical consequence for determining the ionospheric electric field for our purposes.

[20] Joule heating was calculated using the *F* region electric field obtained from the 30° zenith angle ESR ion velocities and *E* region Pedersen conductance obtained from the 56° zenith angle ESR synthesized plasma densities (see Figure 3). The latter were integrated over 95–145 km altitude. The altitude is 74 and 128 km at the SCANDI sector boundaries, i.e., 110 and 190 km radius, respectively. Hence for the higher altitudes up to 145 km, the ESR data unavoidably extends beyond the SCANDI sector boundary (by ~25 km). It was not possible to extend the conductance calculation to higher heights, with 145 km altitude corresponding to a range of 260 km, because the ESR reached its detection limit. Increasing the integration time from $2 \times 6.4 = 12.8$ s is not feasible because of the continuous dish motion. Hence although the absolute Pedersen conductance and therefore Joule heating values will be too low, their relative values will remain correct. Figures 4a, 4b, and 4c show the spatial distribution of Pedersen conductance in 22.5° sectors about Longyearbyen for 2312–2330, 2336–2354, and 2436–2454 UT. Figures 5a, 5b, and 5c show the spatial distribution of Joule heating in the same format. Figures 4b and 4c and Figures 5b and 5c also show the location of the visible auroras mapped at 110 km altitude. Clearly, the auroras partly intersect with some of the ESR's data, which came from greater ranges than indicated by the data sectors (as discussed above). Table 1 gives the Pedersen conductance, electric field, Joule heating, and *E* region neutral temperature for each sector, with average uncertainties of 4.3%, 19.3%, 35.8%, and 0.7% over all the study periods. The average uncertainty for each time period is given in Table 1. The average value and maximum percentage change is also given for each time period. The low neutral temperature uncertainty comes about because of the larger 45° SCANDI sector area (see Figure 1) and long integration time (7 min).

[21] Figure 6 shows the ion-neutral collision frequency calculated from equation (8) using the fitted ion and neutral vector data averaged over the entire sky for 2436–2454 UT (see Figures 2c and 2e) after the aurora had mostly disappeared. For this specific time period, we estimate the

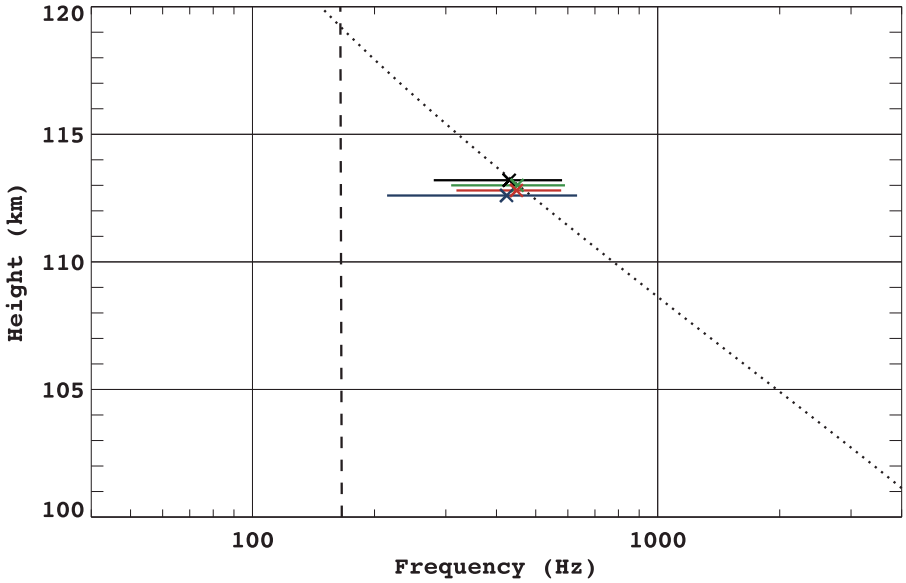

Figure 6. The estimated value of ion-neutral collision frequency at 112.8 km altitude using the east-west (black) and north-south (green) neutral wind vector components as well as the vector magnitudes (red) and angles (blue). Also shown are equation (3) for ion-neutral collision frequency (dotted line) and ion cyclotron frequency (dashed line).

effective 557.7 nm altitude was 112.8 ± 0.8 km. Since the ion-neutral collision frequency emerges from a vector calculation, it can be done independently for orthogonal components [cf. *Davies et al.*, 1997]. This has been done referring to the east-west (black) and north-south (green) neutral wind components as well as the vector magnitudes (red) and angles (blue) separately before averaging. The ion-neutral collision frequency is in the range 424–450 Hz (average 438 Hz) with an uncertainty of 36% (±79 Hz). The average uncertainty in the *F* region ion flow is 19%, and in the *E* region ion and neutral flow uncertainties are 16% and 29%, respectively. The average neutral wind uncertainty is greatest because there are fewer vectors (i.e., larger sectors) over the entire sky than ion flow vectors. Figure 6 also shows the ion-neutral collision frequency from equation (3) (dotted line) and ion cyclotron frequency (dashed line) with altitude. These are equal at ~119 km altitude. The ion-neutral collision frequency calculation could not be done for 2312–2330 UT, prior to when the aurora appeared, due to a lack of suitable ion and neutral flow data (signal too low). Applying equation (8) during 2336–2354 UT, when the aurora was present around much of the horizon, resulted in many unrealistic, including some negative, values. This may be due to the time taken for the ESR to complete a scan for not perfectly stationary aurora as well as 557.7 nm height variations due to the obvious structure of the aurora. Even for 2436–2454 UT, which corresponds to a quiet period with aurora present only on the south and southeast horizon (see Figures 2c and 2e), it was not possible to extract the ion-neutral collision frequency from individual 45° sectors corresponding to the SCANDI data because the uncertainties become very large without averaging over the entire sky.

[22] The raw data measurement uncertainties for the ESR are obtained from the GUISDAP incoherent backscatter spectrum-fitting algorithm [*Lehtinen and Huuskonen*, 1996]. The same is true when extracting basic parameters from the SDI data [cf. *Anderson et al.*, 2009]. However, when calculating physical parameters such as Joule heating (equation (1)), Pedersen conductance (equation (2)), and ion-neutral collision frequency (equation (8)), the uncertainty (δ) for a physical parameter (f) is estimated by propagating the uncertainties of the measured input data (x, y, …) by using $\delta_f^2 = (\partial f/\partial x)^2 \cdot \delta_x^2 + (\partial f/\partial y)^2 \cdot \delta_y^2 + \ldots$. We have assumed zero uncertainty for modeled input data (e.g., geomagnetic field from IGRF and neutral density from MSIS). The Pedersen conductance calculation uses an estimate of the electron-neutral collision frequency, which requires knowledge of the electron temperature. However, owing to the high uncertainty in the ESR-derived temperature data, which is a direct result of the low plasma density in the *E* layer, we have used MSIS values of neutral temperature instead of the measured electron temperatures. This approach is justified in the lower *E* region for quiet geomagnetic conditions. We have not used the SDI measurement of the neutral temperature because this is effectively valid for one altitude only.

3. Results and Discussion

[23] Figure 2a for before the appearance of the aurora shows an empty sky overhead, except for some aurora on the southeast horizon. Figures 2c and 2e for after the appearance of the aurora also show essentially an empty sky overhead, except for some aurora on the southern and southeast horizon. Figures 2b and 2d are for the most stable period of aurora and show optical emissions stretching across most of the northern sky and part of the southwest horizon. The *F* region ion flow was equatorward during 2312–2330 UT (Figure 2a), giving a westward electric field, turned eastward when the aurora appeared during 2336–2354 UT (Figure 2b) and remained eastward with reduced strength after the aurora mostly disappeared during 2436–2454 UT (Figure 2c), giving an equatorward electric field of the dawn convection cell, as

expected. The ESR *F* region flows and their changes are consistent with SuperDARN ionospheric convection (not shown). We do not believe that the aurora changed the *F* region ion flow direction when it appeared; it is more likely that this is merely coincidence. The *E* region ion flow is mostly southeastward and the neutral flow mostly eastward (Figures 2d and 2e). These are consistent with each other. There is no dramatic change after the aurora disappears. We do not have reliable *E* region ion and neutral flow data prior to the appearance of the aurora. Hence it is not possible to determine whether either changed their direction with the appearance of the aurora, as has been reported by *Kosch et al.* [2010] for the *E* region neutral winds. We note that the *F* region ion flows have larger amplitude than *E* region ion flows, which in turn have larger amplitude than the *E* region neutral winds, which is expected. Perhaps surprisingly, the rotation of the *E* region ion flows toward the electric field direction, i.e., 90° clockwise to the *F* region ion flow, is not very apparent for 2336–2354 UT (Figure 2d). In the lower *E* region, a ~45° rotation relative to the *F* region is expected where the ion-gyro and ion-neutral collision frequencies are approximately equal [cf. *Brekke et al.*, 1990; *Brekke*, 1997]. This is apparent for 2436–2454 UT (Figure 2e). According to Figure 6, this condition occurs at ~119 km over Longyearbyen, which is nevertheless above our height estimate of 112.8 ± 0.8 km for this time period. The modest angle between *F* and *E* region ion flow indicates that a neutral wind is present in the *E* region flowing approximately parallel to the *F* region ion flow. Figures 2b and 2d, as well as Figures 2c and 2e, show this to be the case. A small angle between *F* and *E* region ion flow can also indicate a lower than expected neutral density, which is feasible given our late winter nighttime experiment toward the end of solar minimum and is consistent with satellite observations [e.g., *Emmert et al.*, 2010; *Heelis et al.*, 2009].

[24] The neutral temperature data given in Table 1 show a maximum variation of 22% around the analysis annulus for both 2336–2354 and 2436–2454 UT, indicating that the effective height variation of the 557.7 nm emission over 360° was probably low and reasonably well constrained within one scale height (±5 km) of 110 km altitude. However, there are some possible localized issues with the aurora not being entirely stationary. For example, in Figure 2d, near the north-northwest horizon there is a patch of brighter aurora that corresponds to an *E* region ion flow vector not pointing in the same general direction as its neighbors. There is also a faint aurora near the zenith in the southwest sector of Figure 2d, which may account for the discontinuity in low zenith angle ion flow south of zenith. In Figure 2e, there is a faint aurora present between the ESR data rings in the southwest quadrant, which may explain the sudden change in direction of *E* region ion flow in the high zenith angle ion flow. Such problems are unavoidable and we have chosen the best available time periods for the analysis. In addition, there are potential temporal ambiguity issues associated with the slowness of the radar scan cycle (17.8 min). This is particularly clear in Figure 2b where the average ion flow magnitude for the high and low zenith angle azimuthal ESR scans do not appear equal. A reason that the two data rings may have systematic differences is that the uniform flow component is calculated separately in each ring when performing the vector fit. Unlike the partial derivatives, which are averaged across both rings, the uniform background flow term is allowed to vary between rings. This is explained in detail by *Anderson et al.* [2009]. The situation is somewhat exacerbated in this case study by the radar not following the intended dish scan pattern. However, when combining *F* and *E* region data, the slow radar scan is not quite as serious as it may initially seem. We use the inner ESR data ring for the *F* region ion flow, which takes 4 min to scan, and the outer ESR data ring for *E* region ion flow, which takes 12 min to scan. However, *E* region flow is less variable over time simply due to the higher density of the neutrals.

[25] Figures 4a and 5a show low Pedersen conductance (average 0.52 S) and Joule heating (average 0.63 mW/m^2), respectively, despite the relatively high electric fields (average 32.6 mV/m, see Figure 2a) for 2312–2330 UT. This is consistent with very low auroral precipitation. Figures 4b and 5b show high Pedersen conductance (average 2.79 S) and Joule heating (average 4.13 mW/m^2), respectively, along with high electric fields (average 38.1 mV/m, see Figure 2b). This is consistent with the presence of the auroral arcs driving a Pedersen current through the ionosphere [e.g., *Aikio et al.*, 1993; *Lewis et al.*, 1994; *McCrea et al.*, 1991]. We note that the sectors of particularly enhanced Pedersen conductance and Joule heating in the northwest and southwest correspond to the presence of the aurora. Figures 4c and 5c show high Pedersen conductance (average 1.98 S) and low Joule heating (average 0.81 mW/m^2), respectively, along with low electric fields (average 19.8 mV/m, see Figure 2c). Again, this is consistent with the postaurora situation. Using the global average empirical formulas for Joule heating by *Kosch and Nielsen* [1995], K_p = 3 and 4 corresponds to 3.33 and 5.83 mW/m^2, respectively. While this is in agreement with our averaged data when the aurora is present (4.13 mW/m^2), the empirical formulas can clearly never reproduce any mesoscale variations. The discrepancy would be less had we been able to integrate the Pedersen conductance above 145 km altitude but not enough to explain the difference.

[26] The CTIP model predicts that we capture 72% of the total Pedersen conductance by cutting off the integration at 145 km. Hence our Pedersen conductance and Joule heating values should be increased by 28% to be more realistic, at least according to CTIP. We do this in order to compare our observations with the CTIP model prediction. For 2312–2330 UT we observe an adjusted average of 0.67 S and 0.81 mW/m^2 and CTIP predicts 4.45 S and 1.22 mW/m^2. The Joule heating agrees reasonably well but the conductance does not. Our lower conductance measurement is consistent with no auroral precipitation. For 2336–2354 UT we observe an adjusted average of 3.57 S and 5.29 mW/m^2 and CTIP predicts 3.02 S and 1.13 mW/m^2. The conductance agrees reasonably well but the large Joule heating discrepancy between observation and model is largely due to the fact that the model cannot take into account the local auroral precipitation. In fact, CTIP predicts less conductance and heating during the aurora than before its appearance, which is clearly incorrect. For 2436–2454 UT we observe an adjusted average of 2.75 S and 1.13 mW/m^2 and CTIP predicts 3.53 S and 0.067 mW/m^2. Here the model predicts a lower heating rate after the aurora mostly disappears, which is correct, but a higher conductance, which is incorrect. Again, the dis-

crepancy between model and observation is large for Joule heating. It is clear that the model cannot reproduce the observations because it does not have the resolution to account for mesoscale variability nor can it account for localized auroral precipitation.

[27] The main point here is the variability of the Joule heating, not its absolute value. For variability comparison purposes only, we exclude those data sectors for which the ESR was pointing into the aurora at 2336–2354 and 2436–2454 UT, i.e., the six northernmost sectors and the two southwest sectors in Figure 5b and four southeastern sectors in Figure 5c, closest to the aurora. In Figures 5a, 5b, and 5c, Joule heating varies by 308%, 90%, and 269%, respectively, over 360° with respect to the average. This variation is large compared to the average measurement uncertainty of 35.8% (see Table 1). Bearing in mind that it takes 30 s to scan two neighboring sectors, the largest change in Joule heating between any pair of neighboring sectors is 278%, 47%, and 201% with respect to the average in Figures 5a, 5b, and 5c, respectively. It is clear that current ionosphere-thermosphere models cannot replicate this variability due to their low spatial and temporal resolution (e.g., CTIP, 2° latitude, 18° longitude, 72 min). The consequence of this is illustrated by the total power dissipated in our analysis annulus, covering 110 to 190 km radius (see Figure 3). The total area covered by the annulus is 7.54×10^{10} m^2 and by each 22.5° sector is 4.71×10^9 m^2. Using the average electric field and Pedersen conductance, the total power dissipated is 4.16×10^7, 3.05×10^8, and 5.82×10^7 W for Figures 5a, 5b, and 5c, respectively. However, if we integrate the power dissipated in each sector, giving the same total area, then the total power dissipated is 4.74×10^7, 3.12×10^8, and 6.10×10^7 W for Figures 5a, 5b, and 5c, respectively. This means that the total power dissipated, when integrated over smaller sectors, results in a 13.9%, 2.3%, and 4.8% increase for Figures 5a, 5b, and 5c, respectively. Perhaps surprisingly, the discrepancy is smallest when the electric field and conductance is high (Figures 2b and 4b) and greatest for low conductance and high electric field (Figures 2a and 4a). Of course, the Pedersen conductance and electric field are coupled as higher Pedersen conductance tends to short out the electric field. While we cannot draw a general conclusion from this one case study, it seems clear that large-scale spatial averaging results in the underestimation of energy dissipation, which is consistent with *Codrescu et al.* [1995, 2000] and *Rodger et al.* [2001] findings, although the discrepancy for our case study is within the measurement uncertainty for Joule heating (35.8%). From our experiment it is not possible to determine the smallest sector size that would give an accurate determination of the total power dissipated because reducing the sector size results in increased measurement uncertainty. However, it is probably less than our sector size of 64 km. From this case study, it seems clear that current thermosphere-ionosphere models cannot possibly accurately determine the total power dissipated in the upper atmosphere as none can achieve mesoscale resolution.

[28] The ion-neutral collision frequency shown in Figure 6 has an average value of 438 Hz, whereas equation (3) predicts 471 Hz at 112.8 km altitude using the MSIS model, a discrepancy of 33 Hz which is within the measurement uncertainty (±79 Hz). The predicted ion-neutral collision frequency varies rapidly with altitude in the *E* region, changing by almost an order of magnitude within one scale height (~10 km). To get good agreement, our altitude estimate of the 557.7 nm emission would have to be ~113.2 km, which is entirely feasible given our measurement uncertainty of ±0.8 km. The ±79 Hz uncertainty in the ion-neutral collision frequency estimate corresponds to a height range of about 1 km around 113 km according equation (3), i.e., much less than one scale height. Since our height estimate is 112.8 ± 0.8 km, it appears that our observational estimate of the *E* region ion-neutral collision frequency is good agreement with that derived from MSIS. However, an unquantified source of uncertainty is the effect of the *F* region neutral winds on our ionospheric electric field estimate. The application of equations (3) and (8) offers the possibility to make mesoscale measurements of neutral density. Given the observations of large and sustained vertical neutral winds [e.g., *Price et al.*, 1995; *Rees et al.*, 1984; *Smith*, 1998], often in association with auroral activity and Joule heating, it seems probable that the neutral composition and density should be variable near auroral arcs. Future observations are needed to study this.

[29] There is no doubt that the slowness of the radar scan is a fundamental limitation for this experiment. However, with a single dish radar, there are few options. Even if increasing the scan rate were possible, the integration time per sector would decrease resulting in lower signal-to-noise ratio of the data. Given the mechanical speed and high zenith angle pointing limitations of the ESR, a future experiment should only have azimuthal scans at two zenith angles, thereby reducing the total scan time to ~9 min for the mesoscale Joule heating estimate and avoiding the cable wind-up problem. In addition, the passive SDI observations mean that experimenters have no control over the effective height of the data in the *E* layer, which will always be determined by the energy of the auroral precipitation producing the 557.7 nm emission (see equation (9)).

4. Conclusion

[30] Using a novel dish scan mode on the EISCAT Svalbard radar, combined with all-sky *E* region neutral wind observations from a scanning Doppler imager, we have made mesoscale observations of ion and neutral flow, partly in the vicinity of an auroral arc, within the polar cap at ~110 km altitude. We show that Joule heating can vary by >100% within 64 km horizontal distance. It is clear that current ionosphere-thermosphere general circulation models are far from realizing such mesoscale variability, which probably accounts for at least part of their underestimation of the ionosphere-magnetosphere energy coupling budget. We also perform the first estimate of the *E* region ion-neutral collision frequency at 112.8 (±0.8) km altitude by combining *E* and *F* region ion flow with *E* region neutral flow data. Our result is in good agreement with the ion-neutral frequency derived from the MSIS atmospheric model.

[31] **Acknowledgments.** M.J.K. acknowledges funding support for his Visiting Professorship at the Solar-Terrestrial Environment Laboratory of Nagoya University. The CTIP model was run through the Community Coordinated Modeling Centre (http://ccmc.gsfc.nasa.gov). EISCAT is an international association supported by research organizations in China

(CRIRP), Finland (SA), Germany (DFG), Japan (NIPR and STEL), Norway (NFR), Sweden (VR), and the United Kingdom (NERC). We are grateful to G. O'Connor for assistance in producing the figures.

[32] Robert Lysak thanks the reviewers for their assistance in evaluating this paper.

References

Ahn, B.-H., et al. (1983), The Joule heat production rate and the particle energy injection rate as a function of the geomagnetic indices AE and AL, *J. Geophys. Res.*, *88*, 6275–6287, doi:10.1029/JA088iA08p06275.

Aikio, A. T., and A. Selkälä (2009), Statistical properties of Joule heating rate, electric field and conductances at high latitudes, *Ann. Geophys.*, *27*, 2661–2673, doi:10.5194/angeo-27-2661-2009.

Aikio, A. T., et al. (1993), Ground-based measurements of an arc-associated electric field, *J. Atmos. Terr. Phys.*, *55*, 797–808, doi:10.1016/0021-9169(93)90021-P.

Akasofu, S.-I. (1981), Energy coupling between solar wind and the magnetosphere, *Space Sci. Rev.*, *28*, 121–190, doi:10.1007/BF00218810.

Anderson, C., et al. (2009), Thermospheric winds and temperatures above Mawson, Antarctica, observed with an all-sky imaging Fabry-Perot spectrometer, *Ann. Geophys.*, *27*, 2225–2235, doi:10.5194/angeo-27-2225-2009.

Armstrong, J. C., et al. (1975), A comparison of satellite observations of Birkeland currents with ground observations of visible aurora and ionospheric currents, *J. Geophys. Res.*, *80*, 575–586, doi:10.1029/JA080i004p00575.

Arnoldy, R. L. (1974), Auroral particle precipitation and Birkeland currents, *Rev. Geophys.*, *12*, 217–231, doi:10.1029/RG012i002p00217.

Aruliah, A. L., et al. (1991), The combined effect of solar and geomagnetic activity on high latitude thermospheric neutral winds. Part I. Observations, *J. Atmos. Terr. Phys.*, *53*, 467–483, doi:10.1016/0021-9169(91)90075-I.

Aruliah, A. L., et al. (2004), First tristatic studies of meso-scale ion-neutral dynamics and energetics in the high-latitude upper atmosphere using collocated FPIs and EISCAT radar, *Geophys. Res. Lett.*, *31*, L03802, doi:10.1029/2003GL018469.

Aruliah, A. L., et al. (2010), SCANDI–an all-sky Doppler imager for studies of thermospheric spatial structure, *Ann. Geophys.*, *28*, 549–567, doi:10.5194/angeo-28-549-2010.

Banks, P. M., et al. (1977), Observations of Joule and particle heating in the auroral zone, *J. Atmos. Terr. Phys.*, *39*, 179–193, doi:10.1016/0021-9169(77)90112-X.

Brekke, A. (1997), *Physics of the Upper Polar Atmosphere*, John Wiley, New York.

Brekke, A., and C. L. Rino (1978), High-resolution altitude profiles of the auroral zone energy dissipation due to ionospheric currents, *J. Geophys. Res.*, *83*, 2517–2524, doi:10.1029/JA083iA06p02517.

Brekke, A., et al. (1990), EISCAT UHF studies of ionospheric currents on June 16–17, 1987, *Ann. Geophys.*, *8*, 213–222.

Burch, J. L. (1991), Diagnostics of auroral acceleration mechanisms by particle measurements, in *Auroral Physics*, edited by C.-I. Meng, M. J. Rycroft, and L. A. Frank, pp. 97–107, Cambridge Univ. Press, New York.

Burnside, R. G., et al. (1987), The O^+-O collision cross-section: Can it be inferred from aeronomical measurements?, *Ann. Geophys.*, *5A*, 343–350.

Cierpka, K., et al. (2000), Ion-neutral coupling in the high-latitude *F*-layer from incoherent scatter and Fabry-Perot interferometer measurements, *Ann. Geophys.*, *18*, 1145–1153, doi:10.1007/s00585-000-1145-0.

Codrescu, M. V., et al. (1995), On the importance of *E*-field variability for Joule heating in the high-latitude thermosphere, *Geophys. Res. Lett.*, *22*, 2393–2396, doi:10.1029/95GL01909.

Codrescu, M. V., et al. (1997), Modelling the *F* layer during specific geomagnetic storms, *J. Geophys. Res.*, *102*, 14,315–14,329, doi:10.1029/97JA00638.

Codrescu, M. V., et al. (2000), Electric field variability associated with the Millstone Hill electric field model, *J. Geophys. Res.*, *105*, 5265–5273, doi:10.1029/1999JA900463.

Conde, M., and R. W. Smith (1997), Phase compensation of a separation scanned, all-sky imaging Fabry-Perot spectrometer for auroral studies, *Appl. Opt.*, *36*, 5441–5450, doi:10.1364/AO.36.005441.

Conde, M., and R. W. Smith (1998), Spatial structure in the thermospheric horizontal wind above Poker Flat, Alaska, during solar minimum, *J. Geophys. Res.*, *103*, 9449–9471, doi:10.1029/97JA03331.

Crickmore, R. I. (1995), A study of the thermospheric forces at a high latitude site on two days of differing geomagnetic activity, *J. Atmos. Terr. Phys.*, *57*, 759–773, doi:10.1016/0021-9169(94)00063-T.

Currie, B. W. (1955), Auroral heights over west-central Canada, *Can. J. Phys.*, *33*, 773–779.

Davies, J. A., et al. (1997), Deriving the normalised ion-neutral collision frequency from EISCAT observations, *Ann. Geophys.*, *15*, 1557–1569, doi:10.1007/s00585-997-1557-1.

Davis, C. J., et al. (1995), An optimised method for calculating O^+-O collision parameter from aeronomical measurements, *Ann. Geophys.*, *13*, 541–550, doi:10.1007/s00585-995-0541-x.

del Pozo, C. F., et al. (1997), Ion composition and effective ion recombination rate in the nighttime auroral lower ionosphere, *J. Atmos. Sol. Terr. Phys.*, *59*, 1919–1943, doi:10.1016/S1364-6826(97)00033-3.

Doe, R. A., et al. (1993), Observations of nightside auroral cavities, *J. Geophys. Res.*, *98*, 293–310, doi:10.1029/92JA02004.

Doe, R. A., et al. (1995), Electrodynamic model for the formation of auroral ionospheric cavities, *J. Geophys. Res.*, *100*, 9683–9696, doi:10.1029/95JA00001.

Egeland, A., et al. (1973), *Cosmical Geophysics*, Universitetsforlaget, Oslo.

Emmert, J. T., et al. (2010), Record-low thermospheric density during the 2008 solar minimum, *Geophys. Res. Lett.*, *37*, L12102, doi:10.1029/2010GL043671.

Evans, D. S., et al. (1977), Auroral vector electric field and particle comparisons: 2. Electrodynamics of an arc, *J. Geophys. Res.*, *82*, 2235–2249, doi:10.1029/JA082i016p02235.

Friis-Christensen, E., et al. (1985), Interplanetary magnetic field control of the high-latitude electric fields and currents determined from Greenland magnetometer data, *J. Geophys. Res.*, *90*, 1325–1338, doi:10.1029/JA090iA02p01325.

Fujii, R., et al. (1998), The motion of ions in the auroral ionosphere, *J. Geophys. Res.*, *103*, 20,685–20,695, doi:10.1029/98JA01685.

Fujii, R., et al. (1999), Statistical characteristic of electromagnetic energy transfer between magnetosphere, the ionosphere, and the thermosphere, *J. Geophys. Res.*, *104*, 2357–2365, doi:10.1029/98JA02750.

Fujii, R., et al. (2009), Relations between proton auroras, intense electric field, and ionospheric electron density depletion, *J. Geophys. Res.*, *114*, A09304, doi:10.1029/2009JA014319.

Fuller-Rowell, T. J., and D. Rees (1980), A three dimensional time dependent model of the thermosphere, *J. Atmos. Sci.*, *37*, 2545–2567, doi:10.1175/1520-0469(1980)037<2545:ATDTDG>2.0.CO;2.

Galperin, Y. I. (2002), Multiple scales in auroral plasmas, *J. Atmos. Sol. Terr. Phys.*, *64*, 211–229, doi:10.1016/S1364-6826(01)00085-2.

Griffin, E., et al. (2006), Combined ground-based optical support for the aurora (DELTA) sounding rocket campaign, *Earth Planets Space*, *58*, 1113–1121.

Hedin, A. E., et al. (1977), A global thermospheric model bass on mass spectrometer and incoherent scatter data MSIS: 2. Composition, *J. Geophys. Res.*, *82*, 2148–2156, doi:10.1029/JA082i016p02148.

Heelis, R. A., et al. (2002), Ion and neutral motions observed in the winter polar upper atmosphere, *J. Geophys. Res.*, *107*(A12), 1476, doi:10.1029/2002JA009359.

Heelis, R. A., et al. (2009), Behavior of the O^+/H^+ transition height during the extreme solar minimum of 2008, *Geophys. Res. Lett.*, *36*, L00C03, doi:10.1029/2009GL038652.

Hernandez, G. (1986), *The Fabry-Perot Interferometer*, Cambridge Univ. Press, New York.

Iijima, T., and T. A. Potemra (1976), The amplitude distribution of field-aligned currents at northern high latitudes observed by Triad, *J. Geophys. Res.*, *81*, 2165–2174, doi:10.1029/JA081i013p02165.

Iijima, T., and T. Shibaji (1987), Global characteristics of northward IMF-associated (NBZ) field-aligned currents, *J. Geophys. Res.*, *92*, 2408–2424, doi:10.1029/JA092iA03p02408.

Innis, J. L., et al. (1999), A large vertical wind in the thermosphere at the auroral oval/polar cap boundary seen simultaneously from Mawson and Davis, Antarctica, *J. Atmos. Sol. Terr. Phys.*, *61*, 1047–1058, doi:10.1016/S1364-6826(99)00060-7.

Kamide, Y., and S.-I. Akasofu (1976), The location of the field-aligned currents with respect to discrete auroral arcs, *J. Geophys. Res.*, *81*, 3999–4003, doi:10.1029/JA081i022p03999.

Killeen, T. L., and R. G. Roble (1984), An analysis of the high-latitude thermospheric wind pattern calculated by a thermospheric general circulation model 1. Momentum forcing, *J. Geophys. Res.*, *89*, 7509–7522, doi:10.1029/JA089iA09p07509.

Killeen, T. L., and R. G. Roble (1986), An analysis of the high-latitude thermospheric wind pattern calculated by a thermospheric general circulation model: 2. Neutral parcel transport, *J. Geophys. Res.*, *91*, 11,291–11,307, doi:10.1029/JA091iA10p11291.

Killeen, T. L., and R. G. Roble (1988), Thermospheric dynamics: Contributions from the first 5 years of the Dynamics Explorer program, *Rev. Geophys.*, *26*, 329–367, doi:10.1029/RG026i002p00329.

Knudsen, D. J., et al. (2001), Width and structure of mesoscale optical auroral arcs, *Geophys. Res. Lett.*, *28*, 705–708, doi:10.1029/2000GL011969.

Kosch, M. J., and E. Nielsen (1995), Coherent radar estimates of average high-latitude ionospheric Joule heating, *J. Geophys. Res.*, *100*, 12,201–12,215, doi:10.1029/95JA00821.

Kosch, M. J., and E. Nielsen (2001), Coherent radar estimates of high latitude field-aligned currents: Statistical averages, *Adv. Space Res.*, *27*, 1239–1244, doi:10.1016/S0273-1177(01)00168-5.

Kosch, M. J., et al. (1998), Extrapolating EISCAT height-integrated Pedersen conductivities to other parts of the sky using ground-based auroral images, *Ann. Geophys.*, *16*, 583–588, doi:10.1007/s00585-998-0583-y.

Kosch, M. J., et al. (2000a), A comparison of thermospheric winds and temperatures from Fabry-Perot interferometers and EISCAT radar measurements with models, *Adv. Space Res.*, *26*, 979–984, doi:10.1016/S0273-1177(00)00041-7.

Kosch, M. J., et al. (2000b), A comparison of vertical thermospheric winds from Fabry-Perot interferometer measurements over a 50 km baseline, *Adv. Space Res.*, *26*, 985–988, doi:10.1016/S0273-1177(00)00042-9.

Kosch, M. J., et al. (2001a), High-latitude ground-based observations of the thermospheric ion-drag time constant, *Geophys. Res. Lett.*, *28*, 1395–1398, doi:10.1029/2000GL012380.

Kosch, M. J., et al. (2001b), The importance of conductivity gradients in ground-based field-aligned current studies, *Adv. Space Res.*, *27*, 1277–1282, doi:10.1016/S0273-1177(01)00203-4.

Kosch, M. J., et al. (2010), First *E* region observations of mesoscale neutral wind interaction with auroral precipitation, *J. Geophys. Res.*, *115*, A02303, doi:10.1029/2009JA014697.

Kozlovsky, A., et al. (2005), On the field-aligned currents in the vicinity of prenoon auroral arcs, *Geophys. Res. Lett.*, *32*, L18104, doi:10.1029/2005GL023120.

Kozlovsky, A., et al. (2009), Field-aligned currents of postnoon auroral arcs, *J. Geophys. Res.*, *114*, A03301, doi:10.1029/2008JA013666.

Kurihara, J., et al. (2009), Temperature enhancements and vertical winds in the lower thermosphere associated with auroral heating during the Dynamics and Energetics of the Lower Thermosphere in Aurora (DELTA) campaign, *J. Geophys. Res.*, *114*, A12306, doi:10.1029/2009JA014392.

Larsen, M. F. (2002), Winds and shears in the mesosphere and lower thermosphere: Results from four decades of chemical release wind measurements, *J. Geophys. Res.*, *107*(A8), 1215, doi:10.1029/2001JA000218.

Lehtinen, M. S., and A. Huuskonen (1996), General incoherent scatter analysis and GUISDAP, *J. Atmos. Terr. Phys.*, *58*, 435–452, doi:10.1016/0021-9169(95)00047-X.

Lewis, R. V., et al. (1994), The electrodynamics of a drifting auroral arc, *Ann. Geophys.*, *12*, 478–480.

Link, R., and L. L. Cogger (1988), A reexamination of the O I 6300 A nightglow, *J. Geophys. Res.*, *93*, 9883–9892, doi:10.1029/JA093iA09p09883.

Lockwood, M., et al. (2009), The rise and fall of open solar flux during the current grand solar maximum, *Astrophys. J.*, *700*, 937, doi:10.1088/0004-637X/700/2/937.

Maeda, S., et al. (1999), Momentum balance of dayside *E* region neutral winds during geomagnetically quiet summer days, *J. Geophys. Res.*, *104*, 19,871–19,879, doi:10.1029/1999JA900224.

Maeda, S., et al. (2002), Ion and neutral temperature distributions in the *E* region observed by the EISCAT Tromsø and Svalbard radars, *Ann. Geophys.*, *20*, 1415–1427, doi:10.5194/angeo-20-1415-2002.

Maeda, S., et al. (2005), Comparative study of the high-latitude *E* region ion and neutral temperatures in the polar cap and the auroral region derived from EISCAT radar observations, *J. Geophys. Res.*, *110*, A08301, doi:10.1029/2004JA010893.

Marklund, G., et al. (1982), A study of the dynamics of a discrete auroral arc, *Planet. Space Sci.*, *30*, 179–197, doi:10.1016/0032-0633(82)90088-5.

McCormac, F. G., et al. (1987), Circulation of the polar thermosphere during geomagnetically quiet and active times as observed by Dynamics Explorer 2, *J. Geophys. Res.*, *92*, 10,133–10,139, doi:10.1029/JA092iA09p10133.

McCrea, I. W., et al. (1991), On the identification and occurrence of ion frictional heating events in the high-latitude ionosphere, *J. Atmos. Terr. Phys.*, *53*, 587–597, doi:10.1016/0021-9169(91)90087-N.

Millward, G. H., et al. (1996), A Coupled Thermosphere-Ionosphere-Plasmasphere Model (CTIP), in *Solar Terrestrial Energy Program (STEP) Handbook of Ionospheric Models*, edited by R. W. Schunk, pp. 239–279, Utah State Univ., Logan.

Nozawa, S., and A. Brekke (1999), Studies of the auroral *E* region neutral wind through a solar cycle: Quiet days, *J. Geophys. Res.*, *104*, 45–66, doi:10.1029/1998JA900013.

Nozawa, S., et al. (2005), Mean winds, tides, and quasi-2 day wave in the polar lower thermosphere observed in European Incoherent Scatter (EISCAT) 8 day run data in November 2003, *J. Geophys. Res.*, *110*, A12309, doi:10.1029/2005JA011128.

Nozawa, S., et al. (2006), EISCAT observational results during the DELTA campaign, *Earth Planets Space*, *58*, 1183–1191.

Opgenoorth, H. J., et al. (1990), Region of strongly enhanced perpendicular electric fields adjacent to auroral arcs, *J. Atmos. Terr. Phys.*, *52*, 449–458, doi:10.1016/0021-9169(90)90044-N.

Østgaard, N., et al. (2002), Energy analysis of substorms based on remote sensing techniques, solar wind measurements, and geomagnetic indices, *J. Geophys. Res.*, *107*(A9), 1233, doi:10.1029/2001JA002002.

Phillips, A., et al. (1994), A long-term comparison of middle atmosphere winds measured at Saskatoon (52°N, 107°W) by a medium-frequency radar and a Fabry-Perot interferometer, *J. Geophys. Res.*, *99*, 12,923–12,935, doi:10.1029/94JD00618.

Price, G. D., et al. (1995), Simultaneous measurements of large vertical winds in the upper and lower thermosphere, *J. Atmos. Terr. Phys.*, *57*, 631–643, doi:10.1016/0021-9169(94)00103-U.

Rees, M. H. (1989), *Physics and Chemistry of the Upper Atmosphere*, Cambridge Univ. Press, Cambridge, U. K.

Rees, M. H., and D. Luckey (1974), Auroral electron energy derived from ratio of spectroscopic emissions: 1. Model computations, *J. Geophys. Res.*, *79*, 5181–5186, doi:10.1029/JA079i034p05181.

Rees, D., et al. (1984), The generation of vertical thermospheric winds and gravity waves at auroral latitudes 1. Observations of vertical winds, *Planet. Space Sci.*, *32*, 667–684, doi:10.1016/0032-0633(84)90092-8.

Richmond, A. D., et al. (2003), Winds in the high-latitude lower thermosphere: Dependence on the interplanetary magnetic field, *J. Geophys. Res.*, *108*(A2), 1066, doi:10.1029/2002JA009493.

Rino, C. L., et al. (1977), High-resolution auroral zone *E* region neutral wind and current measurements by incoherent scatter radar, *J. Geophys. Res.*, *82*, 2295–2304, doi:10.1029/JA082i016p02295.

Rodger, A. S., et al. (2001), The variability of Joule heating, and its effects on the ionosphere and thermosphere, *Ann. Geophys.*, *19*, 773–781, doi:10.5194/angeo-19-773-2001.

Russell, C. T., et al. (2010), How unprecedented a solar minimum?, *Rev. Geophys.*, *48*, RG2004, doi:10.1029/2009RG000316.

Schunk, R. W., and A. F. Nagy (2009), *Ionospheres: Physics, Plasma Physics, and Chemistry*, Cambridge Univ. Press, Cambridge, U. K., doi:10.1017/CBO9780511635342.

Schunk, R. W., and J. C. G. Walker (1973), Theoretical ion densities in the lower ionosphere, *Planet. Space Sci.*, *21*, 1875–1896, doi:10.1016/0032-0633(73)90118-9.

Senior, C., et al. (1990), Convection electric fields and electrostatic potential over $61° < \Lambda < 72°$ invariant latitude observed with the European incoherent scatter facility. 2. Statistical results, *Ann. Geophys.*, *8*, 257–272.

Smith, R. W. (1998), Vertical winds: A tutorial, *J. Atmos. Sol. Terr. Phys.*, *60*, 1425–1434, doi:10.1016/S1364-6826(98)00058-3.

Solomon, S. C., et al. (2010), Anomalously low solar extreme-ultraviolet irradiance and theremospheric density during solar minimum, *Geophys. Res. Lett.*, *37*, L16103, doi:10.1029/2010GL044468.

Stiles, G. S., et al. (1980), Prolonged radar observations of an auroral arc, *J. Geophys. Res.*, *85*, 1223–1234, doi:10.1029/JA085iA03p01223.

Störmer, C. (1955), *The Polar Aurora*, pp. 67–80, Oxford Univ. Press, Oxford, U. K.

Tanskanen, E., et al. (2002), Substorm energy budget during low and high solar activity: 1997 and 1999 compared, *J. Geophys. Res.*, *107*(A6), 1086, doi:10.1029/2001JA900153.

Thayer, J. P. (1998), Radar measurements of the electromagnetic energy rates associated with the dynamic ionospheric load/generator, *Geophys. Res. Lett.*, *25*, 469–472, doi:10.1029/97GL03660.

Tsuda, T. T., et al. (2007), An ion drag contribution to the lower thermospheric wind in the summer polar region, *J. Geophys. Res.*, *112*, A06319, doi:10.1029/2006JA011785.

Tsuda, T. T., et al. (2009), Acceleration mechanism of high-speed neutral wind observed in the polar lower thermosphere, *J. Geophys. Res.*, *114*, A04322, doi:10.1029/2008JA013867.

Tsunoda, R. T., et al. (1976), The spatial relationship between the evening radar aurora and field-aligned currents, *J. Geophys. Res.*, *81*, 3791–3802, doi:10.1029/JA081i022p03791.

Vlasov, N. V., et al. (2005), Modeling of airglow and ionospheric parameters at Arecibo during quiet and disturbed periods in October 2002, *J. Geophys. Res.*, *110*, A07303, doi:10.1029/2005JA011074.

Wannberg, G., et al. (1997), The EISCAT Svalbard Radar: A case study in modern incoherent scatter radar system design, *Radio Sci.*, *32*, 2283–2307, doi:10.1029/97RS01803.

Weimer, D. R. (2001), Maps of ionospheric field-aligned currents as a function of the interplanetary magnetic field derived from Dynamics Explorer 2 data, *J. Geophys. Res.*, *106*, 12,889–12,902, doi:10.1029/2000JA000295.

Winser, K. J., et al. (1988), Ion-neutral dynamics in the high latitude ionosphere: First results from the INDI experiment, *J. Atmos. Terr. Phys.*, *50*, 369–377, doi:10.1016/0021-9169(88)90021-9.

Zmuda, A. J., and J. C. Armstrong (1974), The diurnal flow pattern of field-aligned currents, *J. Geophys. Res.*, *79*, 4611–4619, doi:10.1029/JA079i031p04611.

C. Anderson, Department of Physics, La Trobe University, Melbourne, VIC 3086, Australia.

A. Aruliah and I. Yiu, Department Physics and Astronomy, University College London, London WC1E 6BT, UK.

L. J. Baddeley, University Centre in Svalbard, P.O. Box 156, N-9178 Longyearbyen, Norway.

V. Howells and I. W. McCrea, Space Science and Technology Department, Rutherford Appleton Laboratory, Didcot OX11 0QX, UK.

M. J. Kosch and J. A. Wild, Physics Department, Lancaster University, Infolab21, South Drive, Lancaster LA1 4WA, UK. (m.kosch@lancaster.ac.uk)

S. Nozawa and T. Tsuda, Solar-Terrestrial Environment Laboratory, Nagoya University, Chikusa-ku, Furo-cho, Nagoya, Aichi 464-8601, Japan.

Y. Ogawa, National Institute of Polar Research, 10-3 Midoricho, Tachikawa, Tokyo, 190-8518, Japan.